

# Facile Synthesis of $\text{Fe}_3\text{O}_4\text{--SiO}_2$ Nanocomposites for Wastewater Treatment

Muhammad Yaseen, Abbas Khan,\* Muhammad Humayun, Saima Farooq, Nasrullah Shah, Shaista Bibi, Zafar A. K. Khattak, Ata Ur Rehman, Sajjad Ahmad, Shah Masood Ahmad, Mohamed Bououdina, and Habib Ullah\*

Water constitutes  $\approx 70\text{--}90\%$  of the organism's body by mass and is highly important for its survival. Water contains a variety of chemical contaminants introduced by various sectors, resulting in contamination that has a direct impact on the ecosystem. Various approaches are in practice to tackle these issues. Among these, semiconductor photocatalysis appears to be the cutting-edge technology for the degradation of wastewater contaminants. Herein, the fabrication of  $\text{Fe}_3\text{O}_4\text{--SiO}_2$  nanocomposite via facile co-precipitation and Stober methods are reported. Various characterization techniques are employed for the structural elucidation, morphology, crystallinity, and stability of the as-prepared composite. The nanocomposite is employed in catalytic and photocatalytic applications toward the removal of methylene blue (MB) and methyl orange (MO) dyes from a comparative perspective. It is observed that the composite can remove about 93% of MB and 51% of MO within 7 and 6 h, respectively. These findings indicate that the nanocomposite has a higher MB removal effectiveness than the MO. This trend can be accredited to the difference in the chemical structure of both dyes. The nanocomposite is also evaluated for antioxidant and antileishmanial activity, and it is shown to be quite effective even at very low concentrations.

## 1. Introduction

Water contamination is due to the release of various industrial chemicals and agricultural activities and is one of the major environmental problems. Since water is a necessary component of all living species, significant efforts have been made to provide clean water for the environment.<sup>[1–3]</sup> Different types of dyes such as basic, acidic, neutral, disperse, azo, direct, and reactive dyes, etc., exist in the wastewater. The majority of these dyes are hazardous to health, and it is difficult to degrade them. The conventional biological technique has been widely utilized for wastewater treatment. However, this is a time-consuming technique and does not fulfill the requirements of efficient wastewater treatment. Chemical approaches are also utilized but these techniques are expensive and usually produce harmful byproducts. Chemical techniques employ a variety of mechanisms, including electrochemical, advanced oxidation

M. Yaseen, A. Khan, N. Shah, S. Bibi  
Department of Chemistry  
Abdul Wali Khan University Mardan  
Mardan 23200, Pakistan  
E-mail: abbas80@awkum.edu.pk

M. Humayun  
School of Optical and Electronic Information, Wuhan National  
Laboratory for Optoelectronics  
Huazhong University of Science and Technology  
Wuhan 430074, P. R. China

S. Farooq  
Department of Biological Sciences and Chemistry, College of Arts and  
Sciences  
University of Nizwa  
Nizwa 616, Oman


Z. A. K. Khattak  
Institute of Chemistry  
Baghdad-ul-Jadeed Campus  
The Islamia University of Bahawalpur  
Bahawalpur 63100, Pakistan

A. U. Rehman  
Department of Chemistry  
Bacha Khan University Charsadda  
Charsadda 24420, Pakistan

S. Ahmad  
Department of Zoology  
Abdul Wali Khan University Mardan  
Mardan 23200, Pakistan

S. M. Ahmad  
Institute of Chemical Sciences  
University of Peshawar  
Peshawar 25120, Pakistan

A. Khan, M. Bououdina  
Department of Mathematics and Sciences  
Faculty of Humanities and Sciences  
Prince Sultan University  
Riyadh 11586, Saudi Arabia

 The ORCID identification number(s) for the author(s) of this article can be found under <https://doi.org/10.1002/mame.202200695>

© 2023 The Authors. Macromolecular Materials and Engineering published by Wiley-VCH GmbH. This is an open access article under the terms of the Creative Commons Attribution License, which permits use, distribution and reproduction in any medium, provided the original work is properly cited.

DOI: 10.1002/mame.202200695

process (AOP), reduction, ozonation, and the Fenton reaction. Besides, the methods involving physical processes including flocculation, adsorption, ion exchange, membrane filtration, irradiation, adsorption, biosorption, reverse osmosis, ultrafiltration, biodegradation, coagulation, nano-filtration, sedimentation, Fenton process, ozonation, and sonolysis are also utilized.<sup>[4–7]</sup> Recently, the photodegradation of pollutants via the aid of semiconductor metal oxides and their binary and ternary nanocomposites received tremendous attention because they can easily degrade various pollutants into harmless products such as CO<sub>2</sub> and H<sub>2</sub>O.<sup>[8–10]</sup> Among the widely used nanomaterials in photocatalysis, magnetic nanoparticles like Fe<sub>3</sub>O<sub>4</sub> received tremendous interest due to their biocompatibility, stability, high surface area-to-volume ratio, and superparamagnetic characteristics. Furthermore, they are nonporous with higher proficiency and rapidly oxidized in ambient air, which affects their magnetic properties and dispensability.<sup>[11]</sup> In order to stabilize magnetic nanoparticles, they are functionalized with carbon, noble metals, metal oxides, and chitosan via different modification strategies. Silica (SiO<sub>2</sub>), an inert coating material, is also used to reduce toxicity, promote stability, biodegradability, and biocompatibility, and to prevent nanoparticle aggregation.<sup>[12]</sup> Based on the literature, some of the silica-based nanocomposites such as Ag/SiO<sub>2</sub>,<sup>[13]</sup> PdNi/C,<sup>[14]</sup> Au@SiO<sub>2</sub>, and SiO<sub>2</sub>@Au core-shell,<sup>[15]</sup> SiO<sub>2</sub>@Au@GO,<sup>[16]</sup> Zr-SiO<sub>2</sub>,<sup>[17]</sup> NiO/SiO<sub>2</sub>,<sup>[18]</sup> CuO-SiO<sub>2</sub>,<sup>[19]</sup> Al<sub>2</sub>O<sub>3</sub>-SiO<sub>2</sub>,<sup>[20]</sup> TiO<sub>2</sub>-SiO<sub>2</sub>-S,<sup>[21]</sup> Al<sub>2</sub>O<sub>3</sub>-SiO<sub>2</sub>-MgO,<sup>[22]</sup> CoFe<sub>2</sub>O<sub>4</sub>/SiO<sub>2</sub>,<sup>[23]</sup> and Fe<sub>3</sub>O<sub>4</sub>-SiO<sub>2</sub>,<sup>[24]</sup> etc., have been reported and gained interest due to the low refractive index and higher thermal and mechanical stability of SiO<sub>2</sub>.<sup>[25]</sup> However, iron-based composites such as Fe<sub>3</sub>O<sub>4</sub>-SiO<sub>2</sub> are known for their potential applications in drug delivery, biocatalysis, heavy metals removal, photocatalysis, MRI contrast agents, biomolecular separations, biomarker immobilization, etc.<sup>[26]</sup> According to some researchers, different strategies such as Stober technique, aerosol pyrolysis, sol-gel process,<sup>[27]</sup> and micro emulsion<sup>[12]</sup> etc., were employed for the preparation of Fe<sub>3</sub>O<sub>4</sub>-SiO<sub>2</sub> nanocomposites. Among these, Stober method is most commonly used due to the absence of any surfactant.<sup>[28]</sup> Some researchers have worked on the degradation/removal of dyes using Fe<sub>3</sub>O<sub>4</sub>-SiO<sub>2</sub>-based nanocomposites. For instance, Kumar et al.,<sup>[8]</sup> fabricated Fe<sub>3</sub>O<sub>4</sub>@SiO<sub>2</sub>@Ru composite and utilized it in the photodegradation of MO and methyl red (MR) dyes with remarkably high photocatalytic activities, especially in acidic media. Likewise, Tahereh et al.,<sup>[29]</sup> utilized ZnFe<sub>2</sub>O<sub>4</sub>@SiO<sub>2</sub>@Tragacanth composite for the removal of MB. The photocatalytic performance of Fe<sub>3</sub>O<sub>4</sub>@SiO<sub>2</sub>@TiO<sub>2</sub>-Co/rGO was also investigated via the photo-degradation of MB dye.<sup>[30]</sup> Recently, Rong et al.,<sup>[31]</sup> investigated the photocatalytic activity of Fe<sub>3</sub>O<sub>4</sub>@SiO<sub>2</sub>@MOFs for Congo red (CR) and MB dyes degradation and stated that the composite exhibited enhanced photocatalytic activity. Mohammad et al.,<sup>[32]</sup> investigated the photocatalytic activity of

Fe<sub>3</sub>O<sub>4</sub>/SiO<sub>2</sub>/Cu<sub>2</sub>O-Ag (Fe/Si/Cu-Ag) toward MB and rhodamine B (RhB) dyes degradation. Likewise, Masha et al.,<sup>[33]</sup> utilized the Fe<sub>3</sub>O<sub>4</sub>/SiO<sub>2</sub>/α-Fe<sub>2</sub>O<sub>3</sub> composite in the removal of MB dye and the composite revealed enhanced photocatalytic activity. Mommad et al.,<sup>[34]</sup> utilized Ag-doped Fe<sub>3</sub>O<sub>4</sub>@SiO<sub>2</sub>@TiO<sub>2</sub> nanocomposites in photocatalysis for MO degradation which revealed high photocatalytic performance compared to the undoped ones.

It is evident from the literature that various types of SiO<sub>2</sub>-based composites revealed good performance for the removal of various dyes in aqueous media. Inspired by those works, herein, we have synthesized Fe<sub>3</sub>O<sub>4</sub>-SiO<sub>2</sub> nanocomposite via the low-cost and facile co-precipitation route using a Stober method. It has been attempted to develop a magnetically active composite with a narrow bandgap. The degradation of MB and MO dyes was used to assess the catalytic/photocatalytic activity of the as-synthesized nanocomposite. These dyes are color pigments that are highly toxic, carcinogenic, non-biodegradable, and affect human and aquatic life even at low doses, they should be avoided. Thus, removing organic contaminants from water is critical. We investigated that the Fe<sub>3</sub>O<sub>4</sub>-SiO<sub>2</sub> nanocomposite exhibit better adsorption/catalytic activities for MB dye removal under dark and light conditions compared to the MO. The enhanced activities may be due to the different chemical nature, structure, and interaction of dye molecules toward the nanocomposite. The kinetics study and biological activities (antioxidants and antileishmanial) of the nanocomposite were also evaluated. In addition to spurring the development of high-performance catalysts for the efficient removal of pollutants from wastewater, this research may also benefit academics.

## 2. Results and Discussion

### 2.1. UV-Vis Absorption Spectroscopy

The UV-vis absorption studies were carried out by dispersing the Fe<sub>3</sub>O<sub>4</sub>-SiO<sub>2</sub> nanocomposite in absolute ethanol and then subjecting the solution to UV-vis Spectrometer Lambda-25 (PerkinElmer) for analysis. The UV-vis spectra were recorded in the wavelength range of 200–800 nm as shown in **Figure 1a**. The peak observed at 416 nm indicates the formation of Fe<sub>3</sub>O<sub>4</sub>-SiO<sub>2</sub> nanocomposite. Similarly, the UV-vis data was used to estimate the bandgap energy of nanocomposite through the following Tauc plot equation (Equation (1)).

$$(\alpha h\nu)^\gamma = A(h\nu - E_g) \quad (1)$$

where " $\alpha$ " stands for the absorption coefficient, " $h$ " denotes the plank constant, " $\nu$ " denotes the frequency of photons, " $A$ " represents the proportionality constant, " $E_g$ " denote the bandgap energy, " $\gamma$ " denote the electron transition whose values can be taken as 2, 1/2, 2/3, or 1/3, depending on the type of transition. The Tauc plot for the Fe<sub>3</sub>O<sub>4</sub>-SiO<sub>2</sub> nanocomposite is indicated in **Figure 1b**. When  $(\alpha h\nu)^\gamma$  was plotted versus  $(h\nu)$ , a straight line was obtained which demonstrates that the absorption edge is due to the direct allowed transitions. The straight-line intercept corresponds to the optical bandgap ( $E_g$ ). The estimated energy bandgap of Fe<sub>3</sub>O<sub>4</sub>-SiO<sub>2</sub> nanocomposite (1.75 eV) is in agreement with the previous reports<sup>[36,37]</sup> The bandgap energy

H. Ullah  
Department of Engineering  
Faculty of Environment  
Science and Economy  
University of Exeter  
Exeter EX4 4QF, UK  
E-mail: hu203@exeter.ac.uk

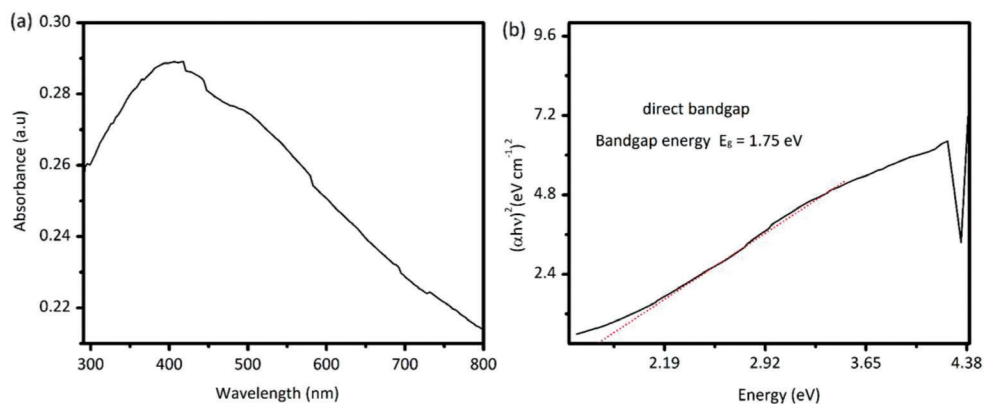


**Figure 1.** a) UV and b) bandgap energy results of  $\text{Fe}_3\text{O}_4\text{-SiO}_2$  nanocomposite.

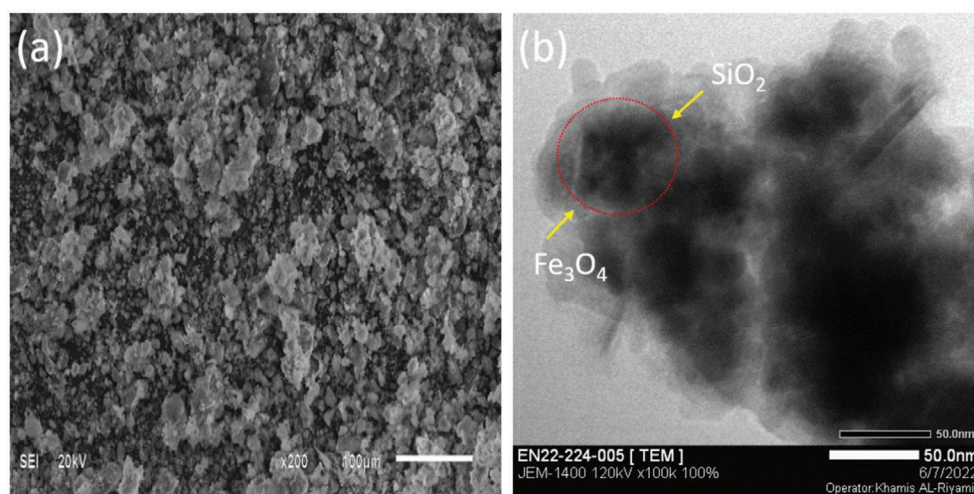


**Figure 2.** a) SEM and b) TEM images of  $\text{Fe}_3\text{O}_4\text{-SiO}_2$  nanocomposite.

( $E_g$ ) values for the  $\text{Fe}_3\text{O}_4\text{-SiO}_2$  are reported in the range of  $E_g = 1.453\text{--}2.047\text{ eV}$ <sup>[35]</sup> and  $E_g = 2.21\text{ eV}$ <sup>[36]</sup>

## 2.2. SEM and TEM Analysis

To study the morphology of the as-synthesized nanocomposite, the scanning electron microscope (SEM; JEOL JSM-7001F) and transmission electron microscope (TEM; HR-TEM, JEOL JEM-3010) instruments were employed. **Figure 2a** shows the SEM micrograph of the nanocomposite which clearly reflects that the magnetic nanoparticles ( $\text{Fe}_3\text{O}_4$ ) are homogeneous and well dispersed in the polymeric silica ( $\text{SiO}_2$ ) matrix, confirming the formation of  $\text{Fe}_3\text{O}_4\text{-SiO}_2$  nanocomposite. Similarly, **Figure 2b** reveals the TEM micrograph of the synthesized nanocomposite material. The dark black color represents the magnetic nanoparticles while the light-dark color corresponds to the polymeric  $\text{SiO}_2$  particles. Here, the magnetic nanoparticles act as the core, and the polymeric  $\text{SiO}_2$  as the shell. The magnetic nanoparticles are coated by the  $\text{SiO}_2$  nanoparticles and led to the successful formation of  $\text{Fe}_3\text{O}_4\text{-SiO}_2$  nanocomposite.

## 2.3. Energy Dispersive X-Ray Analysis

The elemental composition of the sample was confirmed via energy-dispersive X-ray spectroscopy (EDX). EDX results of the  $\text{Fe}_3\text{O}_4\text{-SiO}_2$  nanocomposite are shown in **Figure 3**. The EDX result clearly demonstrates the corresponding peaks of Fe, O, and Si elements. The atomic and mass percentage composition of the Fe, Si, and O elements are provided in **Table 1**. The mass percentage follows the order  $\text{O} > \text{Fe} > \text{Si}$ . This result confirms the successful fabrication of the  $\text{Fe}_3\text{O}_4\text{-SiO}_2$  nanocomposite.

## 2.4. FTIR and XRD Analysis

Fourier transform infrared (FTIR) analysis of the synthesized nanocomposite was monitored through a Perkin Elmer series 100 FT-IR spectrometer with a resolution of  $5\text{ cm}^{-1}$  within the wavenumber range of  $4000\text{--}400\text{ cm}^{-1}$ . The FTIR spectra are depicted in **Figure 4a**. It is found that the band observed at  $451\text{ cm}^{-1}$  is due to the Fe–O stretching vibration. The characteristic peak at  $793\text{ cm}^{-1}$  corresponds to the Si–O–Si bending mode of vibration

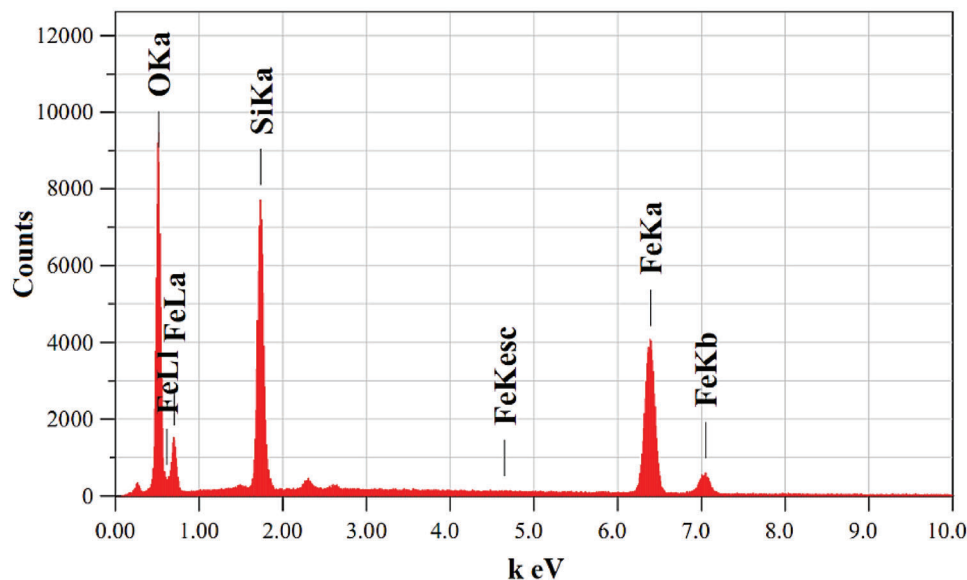


**Figure 3.** EDX image of Fe<sub>3</sub>O<sub>4</sub>-SiO<sub>2</sub> nanocomposite.

**Table 1.** The elemental composition of Fe<sub>3</sub>O<sub>4</sub>-SiO<sub>2</sub> nanocomposite from EDX.

Element	Mass [%]	Atomic [%]
O K	23.27	45.16
Si K	22.15	24.49
Fe K	54.58	30.35

and symmetric stretching vibration. The band at 1073 cm<sup>-1</sup> is due to the asymmetric stretching vibration of Si-O-Si linkage. The absorption band at 1633 cm<sup>-1</sup> corresponds to the H-O-H bending vibration. The peak at 3412 cm<sup>-1</sup> is because of the stretching mode of the O-H group of water. Based on the above FTIR results, it is concluded that the synthesized nanocomposite contains both the Fe<sub>3</sub>O<sub>4</sub> and SiO<sub>2</sub> particles, which successfully confirms the formation of Fe<sub>3</sub>O<sub>4</sub>-SiO<sub>2</sub> nanocomposite.

Similarly, for the crystallinity and phase change of Fe<sub>3</sub>O<sub>4</sub>-SiO<sub>2</sub>, the X-ray diffraction (XRD) analysis was performed using an X-ray diffractometer. The X-ray diffractometer has a Cu-Kα radiation source with wavelength (λ) equal to 0.154 056 nm (1.54 056 Å). The XRD analysis of the samples was done in a 2θ values range of 10°–80° as shown in Figure 4b. The results show that the structure of the nanocomposite exhibits a good degree of crystallinity with some degree of amorphousness. This dual behavior is most likely caused by the corresponding Fe<sub>3</sub>O<sub>4</sub> and SiO<sub>2</sub> particles, as evidenced by the peaks. The diffraction peaks at 31°, 37°, 44°, 58°, and 63° correspond to the (220), (222), (400), (511), and (440) planes, respectively. The wider peak in the range of 10° to 31° in the nanocomposite is amorphous in nature which corresponds to the SiO<sub>2</sub> shell that does not affect the Fe<sub>3</sub>O<sub>4</sub> nanoparticles. The crystal structure of the Fe<sub>3</sub>O<sub>4</sub> also does not change due to the SiO<sub>2</sub> layer on the magnetic Fe<sub>3</sub>O<sub>4</sub> core. This is because the final structure is amorphous, no characteristic SiO<sub>2</sub> peaks can be seen in the XRD result. However, the diffraction peaks of Fe<sub>3</sub>O<sub>4</sub>

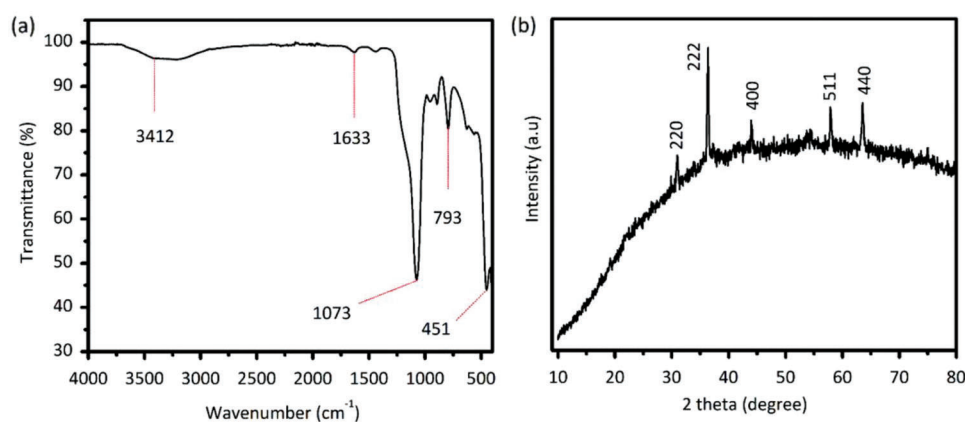


**Figure 4.** a) FTIR and b) XRD spectrum of Fe<sub>3</sub>O<sub>4</sub>-SiO<sub>2</sub> nanocomposite.

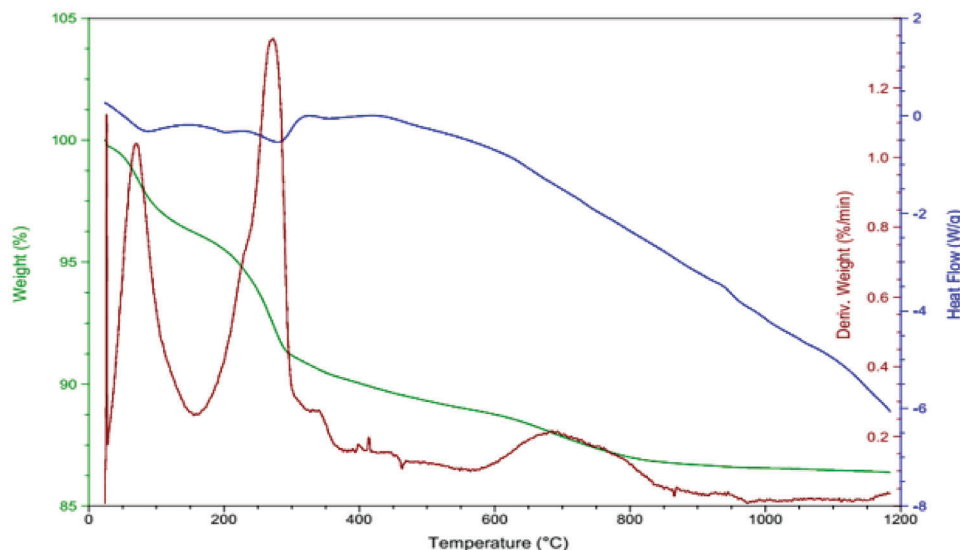


**Figure 5.** TGA/DSC spectra of the  $\text{Fe}_3\text{O}_4\text{-SiO}_2$  nanocomposite.

are not as prominent. This is because the  $\text{SiO}_2$ -coated layer on the surface of the  $\text{Fe}_3\text{O}_4$  core is amorphous. The peaks at  $31^\circ$  to  $63^\circ$  show the crystalline nature of  $\text{Fe}_3\text{O}_4$  nanoparticles in the  $\text{Fe}_3\text{O}_4\text{-SiO}_2$  nanocomposite. This not only indicates the promising fabrication of the  $\text{Fe}_3\text{O}_4\text{-SiO}_2$  nanocomposite but also confirms that the nanocomposites possess both crystalline and amorphous nature.

## 2.5. DSC/TGA Analysis

Thermogravimetric analysis (TGA) was performed in the temperature range of 25 to 800 °C at a rate of  $5^\circ\text{C min}^{-1}$  under  $\text{N}_2$  atmosphere via Shimadzu TG-50 (Japan) thermal analyzer. The differential scanning calorimetry (DSC) analysis was done via the DSC-Q2000 instrument (TA Instrument, New Castle, DE, USA) and differential thermal analysis (DTA) in the range of 50–250 °C under  $\text{N}_2$  atmosphere at  $10^\circ\text{C min}^{-1}$ . The green line represents the TGA (Figure 5), which has three regions ranging in temperature from 148 to 407 °C. A 4% mass loss is observed which could be attributed to the physically adsorbed water or solvent molecules on the surface of the composite material. The mass loss is 11% from 407 to 704 °C due to small molecules desorption, while the mass loss is 2% from 704 to 1200 °C due to the stability of the  $\text{Fe}_3\text{O}_4\text{-SiO}_2$  composite. The blue line in Figure 5 corresponds to the DSC, which shows the endothermic peaks at 81 and 278 °C. This may be due to the crystallization of  $\text{Fe}_3\text{O}_4\text{-SiO}_2$  nanocomposite. On the other hand, an exothermic peak at 316 °C may be due to the stabilization of  $\text{Fe}_3\text{O}_4\text{-SiO}_2$  nanocomposite. The red line in Figure 5 indicates the derivative weight loss% which can give information regarding the exact temperature of various peaks such as 71, 271, and 689 °C.

## 2.6. Photocatalytic Activity

The catalytic and photocatalytic performance of the as-synthesized  $\text{Fe}_3\text{O}_4\text{-SiO}_2$  nanocomposites was evaluated for

MB and MO dye degradation in an aqueous solution at different time intervals. The photocatalytic degradation experiments were carried out in a wooden box, using a 15 W UV lamp as the light source. The inner walls of the box were coated with aluminum foil to avoid the dispersion of light. The photodegradation studies were performed in the presence and absence of a catalyst under light and dark conditions. The degradation experiment proceeded in such a way that the dye solution containing the catalyst was stirred for 30 min to establish equilibrium between the dye molecules adsorbed on the photocatalyst surface. An aliquot of about 7 mL was taken through a syringe from the solution after a regular interval of time, filtered, and examined with the help of a UV-vis spectrophotometer at its  $\lambda_{\text{max}}$ . The degradation percentage of MB and MO was calculated via the following Equation (Equation (2))

$$\text{Removal (\%)} = \left( \frac{A_0 - A_t}{m} \right) \times 100 \quad (2)$$

Where “ $A_0$ ” denotes the initial absorbance and “ $A_t$ ” denotes the final absorbance at a given time interval. To perform the kinetic study of the dye removal process, the given first-order equation (either Equations (3) or (4)) was employed for considering the data.

$$\ln(C_t/C_0) = -k_{\text{app}}t \quad (3)$$

or

$$\ln(A_t/A_0) = -k_{\text{app}}t \quad (4)$$

where “ $C_0$ ” and “ $C_t$ ” stands for the initial and final concentrations of MB and MO dyes at time  $t = 0$  and  $t = t$ . Also, the  $C_0$  and  $A_t$  represent the absorbance at time  $t = 0$  and  $t = t$ . While  $k_{\text{app}}$  represents the apparent rate constant of the reaction estimated from the plots slope  $\ln(A_t/A_0)$  versus time.

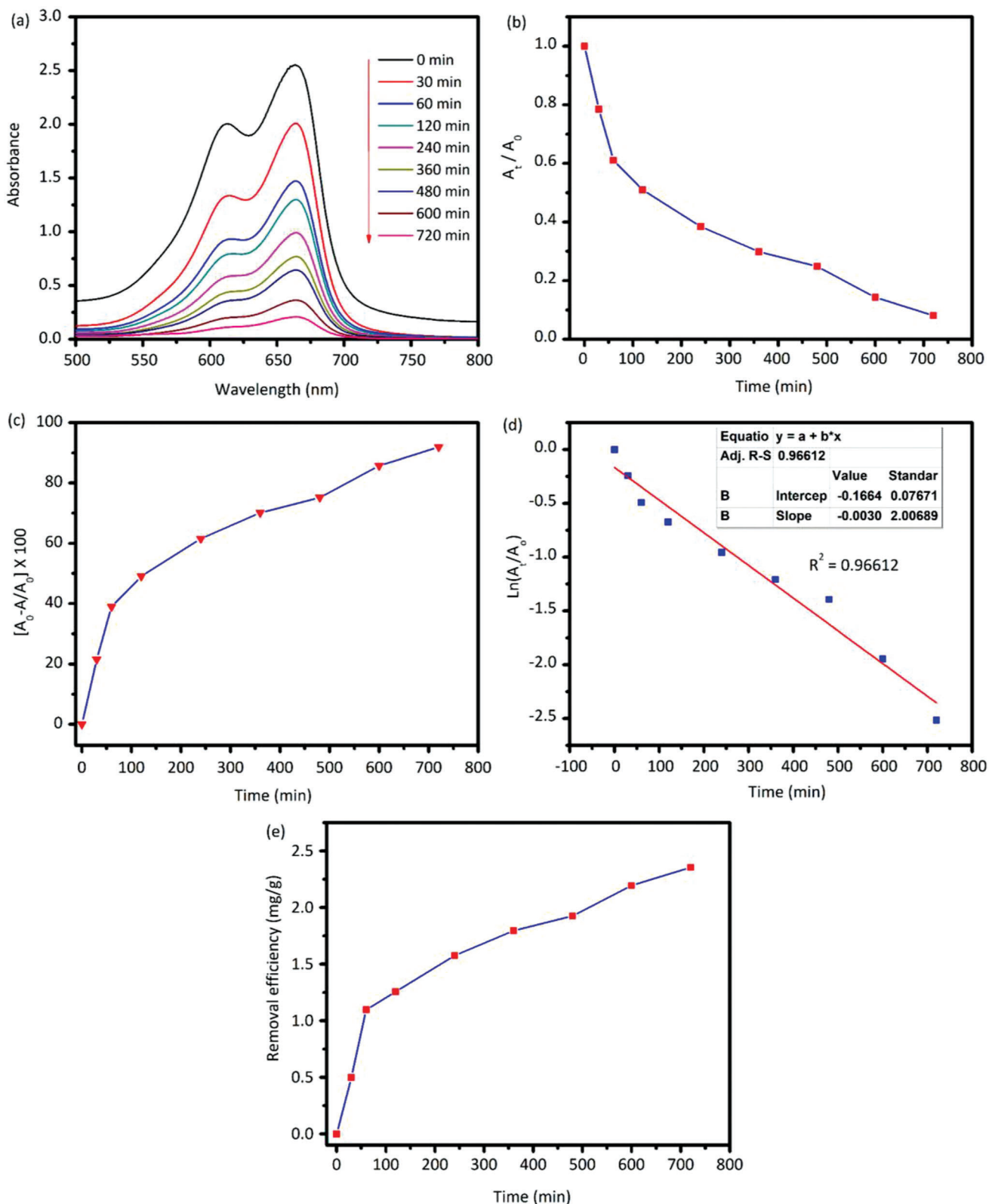


**Figure 6.** MB degradation in the presence and absence of light; a) Difference in UV-vis spectra/absorbance at different time intervals, b) ratio of absorbance ( $A_t/A_0$ ) versus time, c) % decomposition versus time, d) plot of pseudo-first-order kinetics of degradation, and e) removal efficiency.

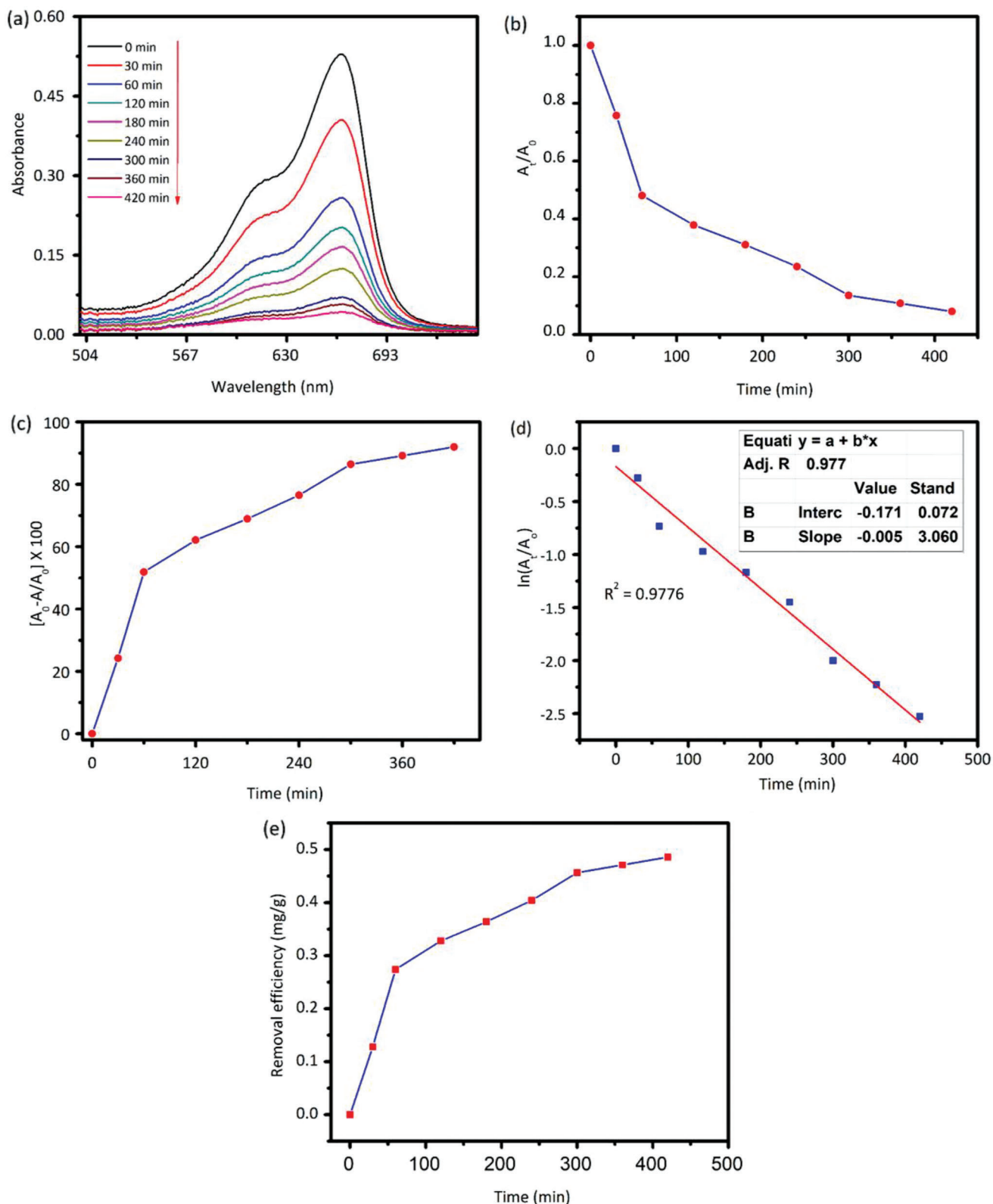


**Figure 7.** Degradation of MB with the aid of 0.1  $\text{Fe}_3\text{O}_4\text{-SiO}_2$  composites under light; a) Changes in the UV-vis absorbance spectra at different time intervals, b) absorbance ratio ( $A_t/A_0$ ) versus time, c) percentage decomposition versus time, d) plot of the pseudo-first-order degradation kinetics, and e) removal efficiency.

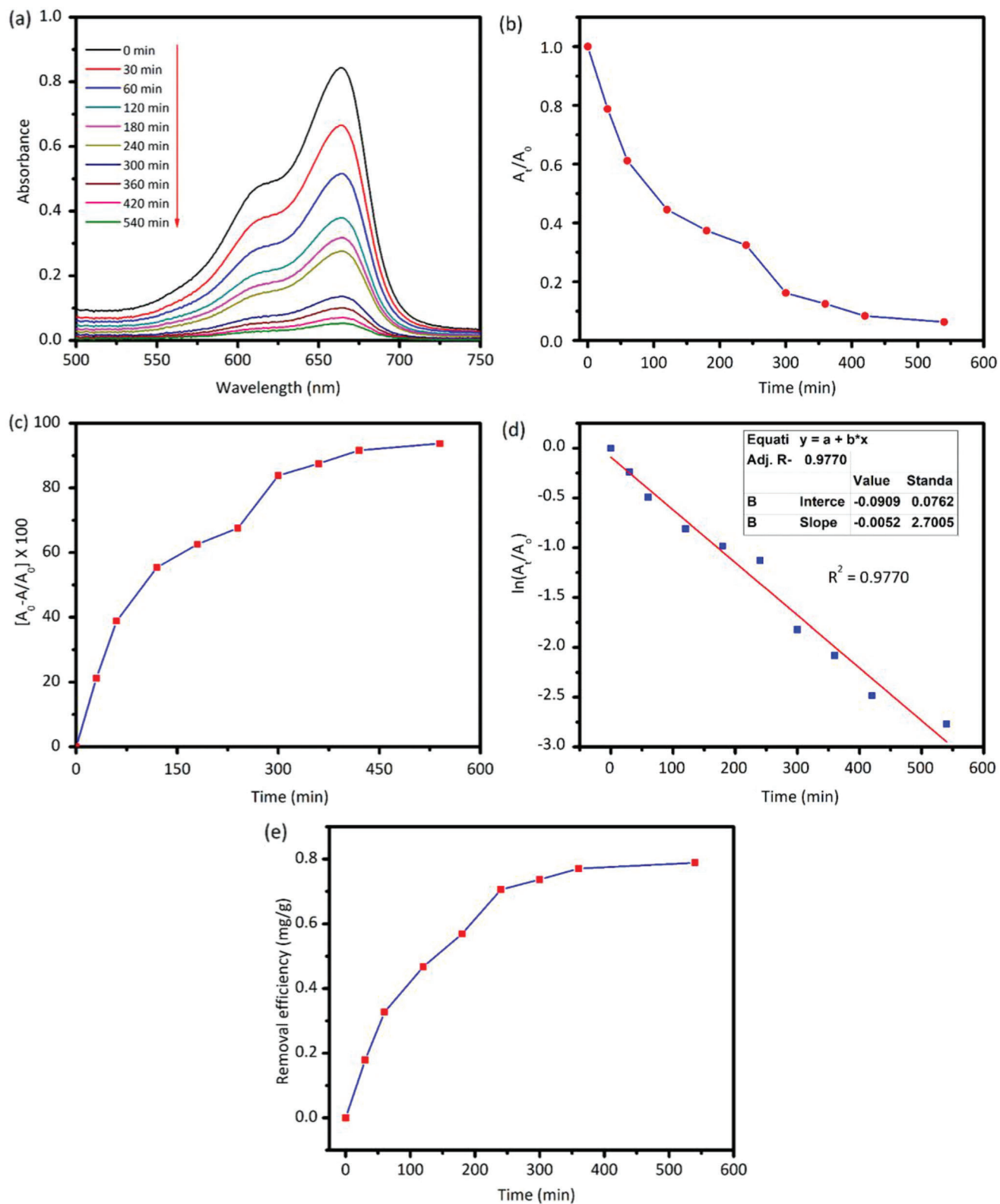


**Figure 8.** MB degradation with the aid of 0.1  $\text{Fe}_3\text{O}_4\text{-SiO}_2$  composites in absence of light (dark condition); a) Change in UV-vis absorbance spectra at different time intervals, b) absorbance ratio ( $A_t/A_0$ ) versus time, c) percentage decomposition versus time, d) plot of pseudo-first-order kinetics of degradation, and e) removal efficiency.



**Table 2.** First-order rate-constant and regression values for the catalytic and photocatalytic degradation of MB.

Catalyst	Dyes	Conditions	Time of experiment [h]	% Removal	R <sup>2</sup> value for first order plot	First order rate constant, k [min <sup>-1</sup> ]
-	MB	Light	12	91	0.966	0.00304
Fe <sub>3</sub> O <sub>4</sub> -SiO <sub>2</sub> (0.1 g)	MB	Light	07	93	0.977	0.00574
Fe <sub>3</sub> O <sub>4</sub> -SiO <sub>2</sub> (0.1 g)	MB	Dark	09	90	0.977	0.00529

The MB degradation along with the time under light is indicated from the plots of absorbance versus the wavelength at different intervals. The degradation progress was confirmed through the decrease in absorbance with time as shown in **Figure 6a**. The degradation process of MB dye can also be observed from the changes occurring in the plot of the ratio of absorbance ( $A_t/A_0$ ) versus time, as shown in **Figure 6b**. As obvious from **Figure 6c**, the percentage decomposition increased with the passage of time. Moreover, **Figure 6d** exhibits the plot of the pseudo-first-order relation for MB degradation. It is clear from the degradation results that the reaction follows a pseudo-first-order equation as indicated by the  $R^2 = 0.96612$ . The first order rate constant ( $K_1$ ) value is equal to  $0.00304 \text{ min}^{-1}$ . **Figure 6e** clearly shows that the removal efficiency increases with the passage of time and reached a maximum at 720 min.

The photocatalytic activity of the synthesized Fe<sub>3</sub>O<sub>4</sub>-SiO<sub>2</sub> composites was investigated by degrading MB under UV-vis light and in dark at various time intervals. It is found that the absorption peak intensity of MB at  $\lambda = 663 \text{ nm}$  decreases with the increase in time. **Figures 7a** and **8a** show the degradation of MB with the Fe<sub>3</sub>O<sub>4</sub>-SiO<sub>2</sub> catalyst in the presence and absence of light, as well as the qualitative and quantitative changes observed using the double UV-vis spectrophotometer. Furthermore, the results revealed that the MB intensity decreases with the increase in the irradiation period. This is due to the gradual degradation of MB molecules with irradiation time. Moreover, the plots in **Figures 7b** and **8b** led us to show that the degradation progress in terms of absorbance ratio ( $A_t/A_0$ ) versus time, demonstrating the degradation of MB dye with Fe<sub>3</sub>O<sub>4</sub>-SiO<sub>2</sub> catalyst takes place by perceiving the quantitative and qualitative fluctuations in spectra with time. This is further confirmed via the percentage decomposition plot versus time. **Figures 7c** and **8c** show that the degradation percentage increases as the time interval increases, as shown by the graphs of decomposition percentage versus time. These findings also show that in the dark, 90% of the dye was removed in 9 h, whereas in the light, a catalyst could remove 93% of the MB in 7 h. **Figures 7d** and **8d** represent the pseudo-first-order relation for the degradation process, confirming that it obeys pseudo-first-order kinetics with acceptable values of  $R^2 = 0.9776$  in light and  $R^2 = 0.9770$  in the absence of light. Moreover, it is found that the removal efficiency increases with the passage of time and reached a maximum at 420 and 540 min, as shown in **Figures 7e** and **8e**. These results indicate that the Fe<sub>3</sub>O<sub>4</sub>-SiO<sub>2</sub> composite has a good efficiency in the removal of MB dye both in the dark and in the light, but it has better activity in the presence of light than in the dark condition. This trend is further supported by the values of the rate constant ( $K_1$ ); as these values for the first-order kinetics were estimated to be 0.00304, 0.00529, and  $0.00574 \text{ min}^{-1}$  for the removal of MB under light without catalyst, in the presence

of a catalyst in dark condition, and under light, respectively (see **Table 2**).

The degradation of the MO dye with time under light irradiation is illustrated by the absorbance versus wavelength plot at regular time intervals as revealed in **Figure 9a**. The progress of MO dye degradation can also be observed by the change in spectra over time, as shown in the plot of absorbance ratio ( $A_t/A_0$ ) versus time in **Figure 9b**. The percent decomposition versus time plot is indicated in **Figure 9c**, revealing that the percent decomposition is increased with the passage of time. Moreover, from **Figure 9d** we can analyze a pseudo-first-order relation for MO degradation. As confirmed from the degradation data, the reaction follows a pseudo-first-order equation as indicated by the  $R^2 = 0.9584$ , with a first-order rate constant ( $K_1$ ) value of  $0.00064 \text{ min}^{-1}$ . The removal efficiency of methyl orange is shown in **Figure 9e**, which clearly demonstrates a continuous increase in the removal efficiency over time, reaching a maximum value in 600 min.

Moreover, the absorbance versus wavelength plots in the dark and in the light for different time intervals of MO dye using Fe<sub>3</sub>O<sub>4</sub>-SiO<sub>2</sub> nanocomposite as a catalyst are depicted in **Figures 10a** and **11a**. The graphs clearly indicate that the intensity of the absorption peak of MO decreases from the maximum wavelength  $\lambda = 464 \text{ nm}$  with the increase in irradiation time. This may be due to the efficient degradation of MO dye molecules over time. The plot of absorbance ratio ( $A_t/A_0$ ) versus time is used for the degradation process as shown in **Figures 10b** and **11b**. Through analyzing the qualitative and quantitative changes in spectra over time, as shown in **Figures 10b** and **11b**, we were able to conclude that MO degradation occurs. **Figures 10c** and **11c** show that the percent decomposition increases over time, as represented by the plot of percent decomposition versus time, and that 50% of dye removal occurred at 10 h in the dark and 51% at 6 h in the light, respectively. Moreover, **Figures 10d** and **11d** indicate the plot of pseudo-first-order relation for MO degradation with Fe<sub>3</sub>O<sub>4</sub>-SiO<sub>2</sub> catalyst. As confirmed, the degradation data follow a pseudo-first-order equation as shown by the  $R^2 = 0.993$ . The first-order rate constant ( $K_1$ ) value is 0.00102 under dark conditions. Similarly, under light conditions, the  $R^2 = 0.985$ , and the first-order rate constant ( $K_1$ ) is equal to 0.002. **Figures 10e** and **11e** clearly show that the removal efficiency increases with the passage of time, reaching a maximum value at 600 and 360 min, respectively.

The “k” values are listed in **Table 3**; where the highest degradation is for methyl orange in the presence of 0.1 g of the composite and under the light. This means that the degradation of MO is faster under the light in the presence of a catalyst compared to the degradation of dye in the dark. Again, this difference in the results well supports the efficient photocatalytic activity of the

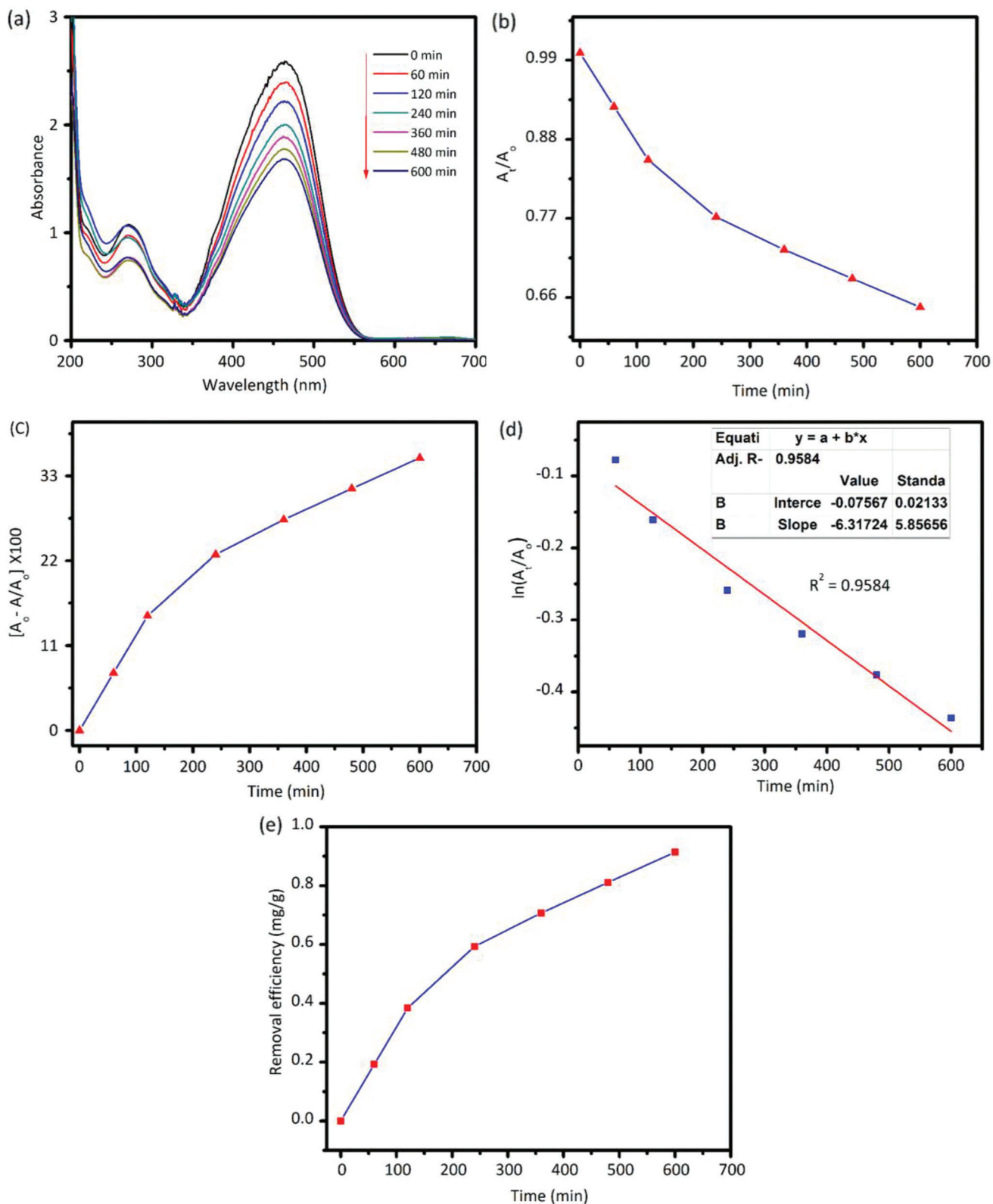


**Figure 9.** Degradation of MO in the presence and absence of light; a) Change in the UV-vis absorbance spectra at different time intervals, b) absorbance ratio ( $A_t/A_0$ ) versus time, c) decomposition percentage versus time, d) plot of pseudo-first-order kinetics of degradation, and e) removal efficiency.

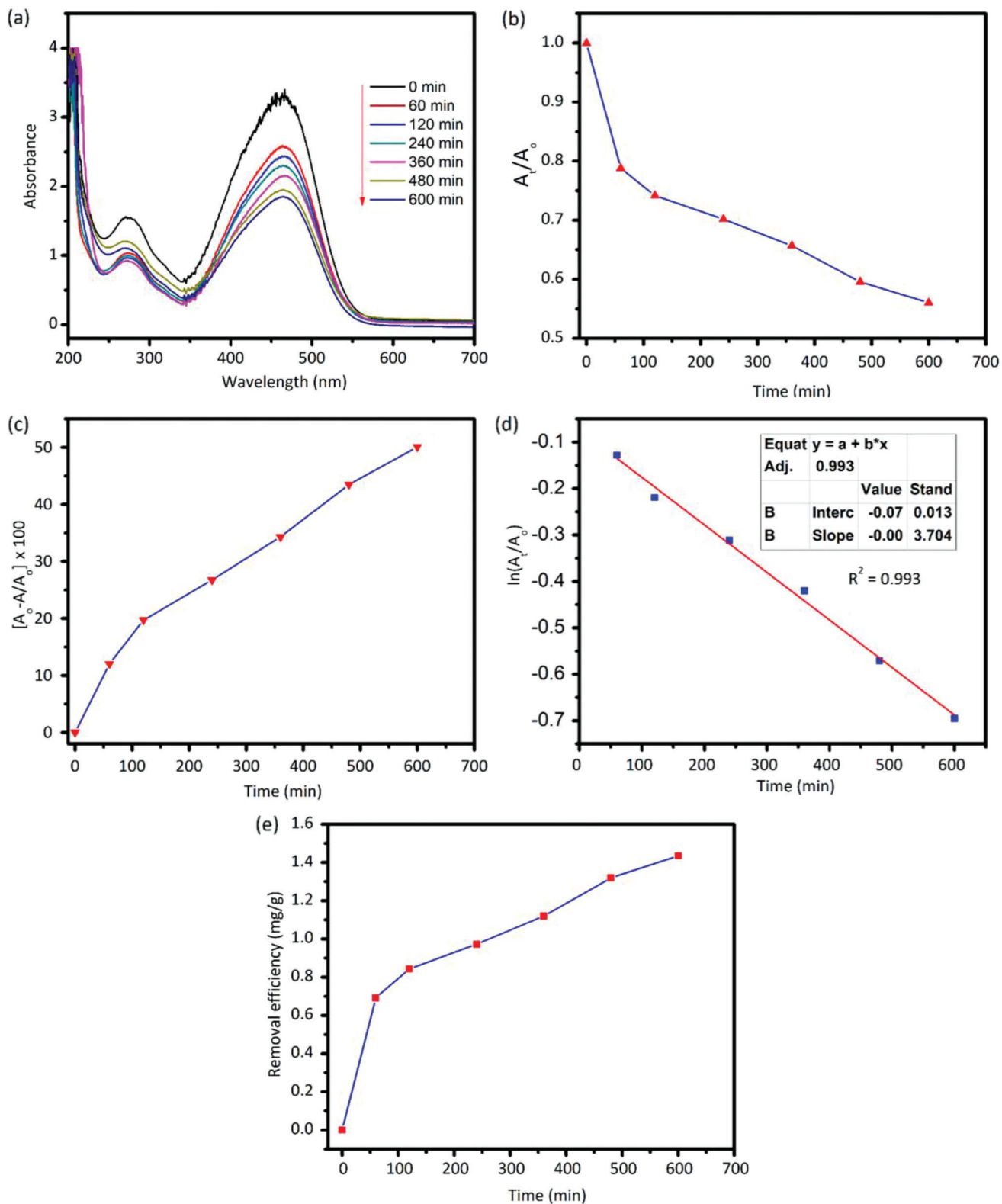


**Figure 10.** MO degradation with the aid of 0.1  $\text{Fe}_3\text{O}_4\text{-SiO}_2$  composites in absence of light (dark); a) Change in UV-vis absorbance spectra at different time intervals, b) absorbance ratio ( $A_t/A_0$ ) versus time, c) decomposition percentage versus time, d) plot of pseudo-first-order kinetics of degradation, and e) removal efficiency.

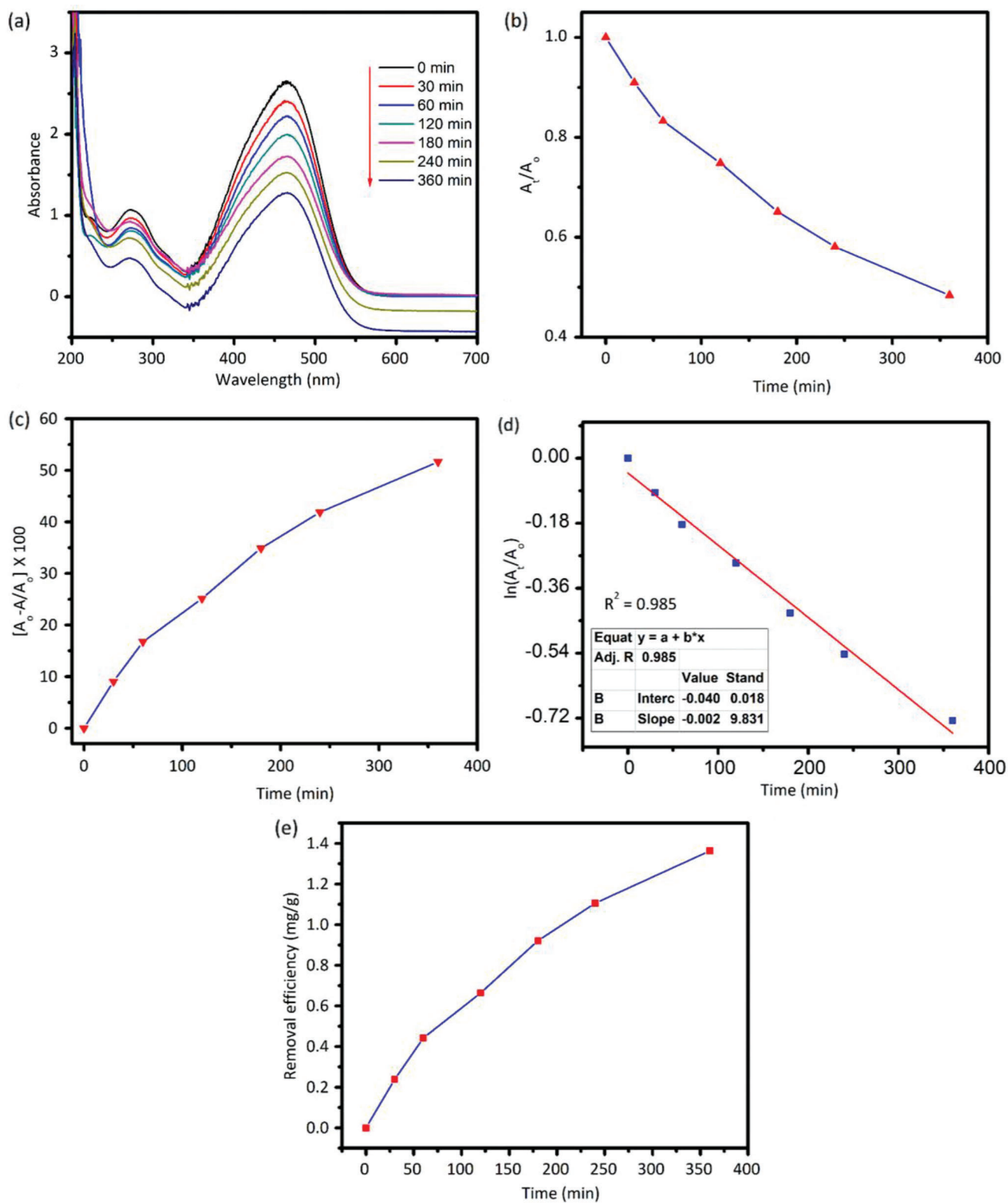


**Figure 11.** MO degradation with the assistance of 0.1 Fe<sub>3</sub>O<sub>4</sub>-SiO<sub>2</sub> composites under light; a) Change in UV-vis absorbance spectra at different time intervals, b) absorbance ratio ( $A_t/A_0$ ) versus time, c) decomposition percentage versus time, d) plot of the pseudo-first-order kinetics of degradation, and e) removal efficiency.

**Table 3.** The first-order rate constant and the regression values for the catalytic and photocatalytic degradation of MO.

Catalyst	Dye	Conditions	Time of experiment [h]	% Removal	R <sup>2</sup> value for first order plot	First order rate constant, k [min <sup>-1</sup> ]
-	MO	Light	10	35	0.958	0.0006
Fe <sub>3</sub> O <sub>4</sub> -SiO <sub>2</sub> (0.1 g)	MO	Dark	10	50	0.993	0.0010
Fe <sub>3</sub> O <sub>4</sub> -SiO <sub>2</sub> (0.1 g)	MO	Light	06	51	0.985	0.0020

**Table 4.** Comparative summary of the removal efficiency of Fe<sub>3</sub>O<sub>4</sub>-SiO<sub>2</sub> composite with those of the recently reported materials.

S.No	Catalyst	Dye	Conditions	% Removal	R <sup>2</sup> value for first order plot	First order rate constant, k [min <sup>-1</sup> ]	Reference
1	-	MB	Light	91	0.966	0.00304	Present work
2	Fe <sub>3</sub> O <sub>4</sub> -SiO <sub>2</sub> (0.1 g)	MB	Light	93	0.977	0.00574	Present work
3	Fe <sub>3</sub> O <sub>4</sub> -SiO <sub>2</sub> (0.1 g)	MB	Dark	90	0.984	0.00529	Present work
4	-	MO	Light	35	0.958	0.00064	Present work
5	Fe <sub>3</sub> O <sub>4</sub> -SiO <sub>2</sub> (0.1 g)	MO	Dark	50	0.993	0.00102	Present work
6	Fe <sub>3</sub> O <sub>4</sub> -SiO <sub>2</sub> (0.1 g)	MO	Light	51	0.985	0.002	Present work
7	Fe <sub>3</sub> O <sub>4</sub> @SiO <sub>2</sub> @TiO <sub>2</sub> -Co/rGO	MB	Visible light	92	0.944	-	[30]
8	Fe <sub>3</sub> O <sub>4</sub> @SiO <sub>2</sub> @MOFs	MB	UV light	90	0.911	-	[31]
9	Fe <sub>3</sub> O <sub>4</sub> /SiO <sub>2</sub> /a-Fe <sub>2</sub> O <sub>3</sub>	MB	UV light	60	-	-	[33]
10	Fe <sub>3</sub> O <sub>4</sub> @SiO <sub>2</sub> @Ru	MO	Visible light	90	-	-	[8]
11	Fe <sub>3</sub> O <sub>4</sub> @SiO <sub>2</sub> @ZnO	MO	UV light	81	-	-	[37]
12	Fe <sub>3</sub> O <sub>4</sub> @SiO <sub>2</sub> @g-C <sub>3</sub> N <sub>4</sub> /TiO <sub>2</sub>	MO	UV light	91	-	-	[38]

catalyst. In addition, the removal of the MO in the dark may be due to the physicochemical adsorption of MO on the surface of the Fe<sub>3</sub>O<sub>4</sub>-SiO<sub>2</sub> composite.

Finally, it can be concluded that the Fe<sub>3</sub>O<sub>4</sub>-SiO<sub>2</sub> nanocomposites exhibit significant catalytic/photocatalytic activity for the removal of MB and MO dyes in the dark as well as in light as can be seen from their *k* values provided in Tables 2 and 3. However, it is observed that under similar experimental conditions, MB could be readily removed compared to the MO. This may be due to the difference in the chemical natures, structures, and ionic nature of the dyes. It can also be analyzed that cationic dye (MB) has greater constructive interaction with the surface of the magnetically active Fe<sub>3</sub>O<sub>4</sub>-SiO<sub>2</sub> core-shell composite compared to the anionic MO. Thus, due to these differences, the mode and strength of dye-substrate interactions with the same catalyst under the same conditions are different. Hence, MB rapidly degrades compared to the MO, as can be seen from their respective *k* values. Another possible reason for this difference is the pH-sensitive nature of the dyes. In this case, a neutral pH of the medium is used, and it is thought that under neutral and/or basic pH conditions, MB can be ionized more readily than MO. It is also expected that under low/acidic pH conditions, the catalyst may acquire a positive charge. And under these conditions, the adsorption of MO onto the surface of the composite may become favorable and the possible removal efficiency of the catalyst would be higher for MO. This overall discussion also supports the better dye removal efficiency of the catalyst toward MB than the MO under neutral pH conditions. A summary of the comparison of our dye removal results with the previously reported data is also presented in Table 4. This clearly indicates that the

as-fabricated Fe<sub>3</sub>O<sub>4</sub>-SiO<sub>2</sub> composite has appreciable dye removal efficiency compared to other materials. It is seen from the overall results that the photocatalytic degradation efficiency of the different experiments varies with changes in the experimental conditions such as catalyst amount, type of catalyst, pollutant concentration, catalyst dose, light source, irradiation time, and chemical structure of the dyes. In addition, the chemical composition, different textures, and morphological properties of the catalyst significantly affect its efficiency. For core-shell materials, it is also important to create materials with a good balance of hydrophilicity and hydrophobicity.

## 2.7. Contribution of Active Species in Photodegradation and Catalyst Recycling

Regarding the role of active species, it is found that the Fe<sub>3</sub>O<sub>4</sub>-SiO<sub>2</sub> composite generates a conduction band via a photocatalytic process. The ability of the catalyst is influenced by the overall properties of the catalyst and the quality of light absorption by the composite. And the generation and type of photogenerated electron-hole pairs at which photocatalytic degradation of the dye is achieved.<sup>[2,6,39]</sup> Reactive charged species such as hydroxyl radical (•OH), superoxide radical (•O<sub>2</sub><sup>-</sup>), and hydrogen peroxide (H<sub>2</sub>O<sub>2</sub>) are known to be involved in the degradation of MB and MO dyes. These reactive species are generated through various methods such as UV light, ozone, hydrogen peroxide, and Fenton's reagent or by some enzymes (e.g., superoxide dismutase). The relative contribution of each active species can also be affected by various factors such as pH, temperature, the presence

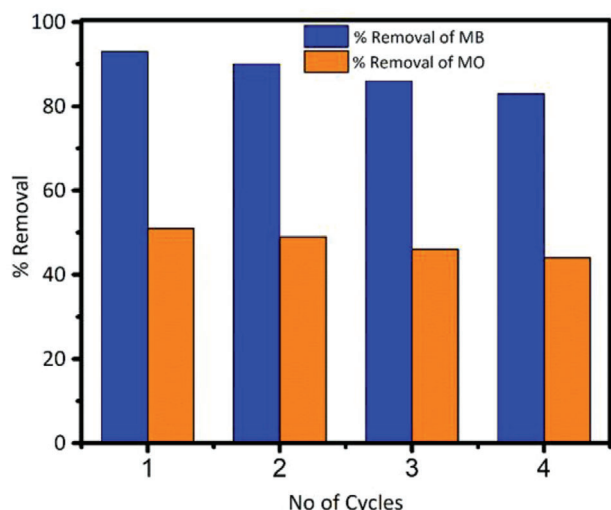


**Figure 12.** Recycling ability of Fe<sub>3</sub>O<sub>4</sub>-SiO<sub>2</sub> composite toward MB and MO dye removal. The concentration of dye 20 mg L<sup>-1</sup>, the amount of catalyst 0.1 g, temperature 25 °C, and time 6 h.

of other oxidants and reductants, and the concentrations of MB and MO. Generally, in the photodegradation process, the charged species migrate to the photocatalyst surface and there the e<sup>-</sup> reduces O<sub>2</sub> to superoxide radicals (<sup>•</sup>O<sub>2</sub><sup>-</sup>) while the h<sup>+</sup> either oxidizes H<sub>2</sub>O to form <sup>•</sup>OH or directly oxidizes MB and MO dyes. These reactive species (<sup>•</sup>O<sub>2</sub><sup>-</sup>, <sup>•</sup>OH, and h<sup>+</sup>) initiate the redox reactions and then degrade the dyes by first oxidizing them through the successive attack of hydroxyl radical <sup>•</sup>OH and /or hole (h<sup>+</sup>). (Dye + (<sup>•</sup>OH or h<sup>+</sup>) → dye<sup>•+</sup> → intermediates.<sup>[2,39]</sup> The intermediates of the dyes produced either undergo self-degradation or transformed by the reactive oxidation species into less harmful byproducts like CO<sub>2</sub>, H<sub>2</sub>O, or inorganic ions. For MB combination, <sup>•</sup>OH/hole is crucial while for MO, formation of the hole (h<sup>+</sup>) plays a vital role. The <sup>•</sup>OH being an important active species for the degradation of MB and MO, attacks on the CS+ =C functional

group. The transformation of the functional group to CS(=O)C occurred and then the main ring constituting the S and N atoms is opened. Similarly, the hole(h<sup>+</sup>) leads to the production of CH and NH linkages. The same is true for MO, but it differently behaves when hole scavengers such as KI are introduced. And the shift in the absorption peaks that appeared may be due to changes in molecular weight and interactions with cationic moieties.<sup>[39,40]</sup> In addition to the difference in the structure, ionic nature, and interaction with catalyst and medium, one of the possible reasons, for the faster degradation of MB in contrast to MO, is the involvement of both holes and hydroxyl radical. While in the case of MO, the formation of holes proved to be the most essential factor.

Furthermore, the stability and performance of the Fe<sub>3</sub>O<sub>4</sub>-SiO<sub>2</sub> composite in terms of the cyclic tests were also evaluated by the removal of both dyes as shown in **Figure 12**. In a typical experiment, the catalyst used in each cycle was recovered, cleaned, and dried in an oven at 100 °C for an hour before being used. A similar process has been used for dye removal and a fixed irradiation time of 6 h for each dye. The percentage removal efficiency was calculated and plotted against the number of cycles. For four continuous cycles, it was revealed that the catalyst's efficiency slightly decreased. This less dramatic change in efficiency could be due to a small amount of material wastage and/or a small alteration to the catalyst's surface. The high recycling efficiency reflects the good stability of the catalyst used in the current experimental setup.

## 2.8. Antioxidant and Antileishmanial Activities

Antioxidant activity of the Fe<sub>3</sub>O<sub>4</sub>-SiO<sub>2</sub> composite was conducted using a DPPH assay, as shown in **Figure 13a** and **Table 5**. In this method, ascorbic acid has been chosen and used as a standard positive control. Notably, as the concentration increases, the antioxidant activity also enhances.<sup>[41,42]</sup> **Figure 13a** shows that at various concentrations of solution, the antioxidant activity is different for the respective nanocomposite. The antioxidant activity of the nanocomposite for various concentrations of the solution is

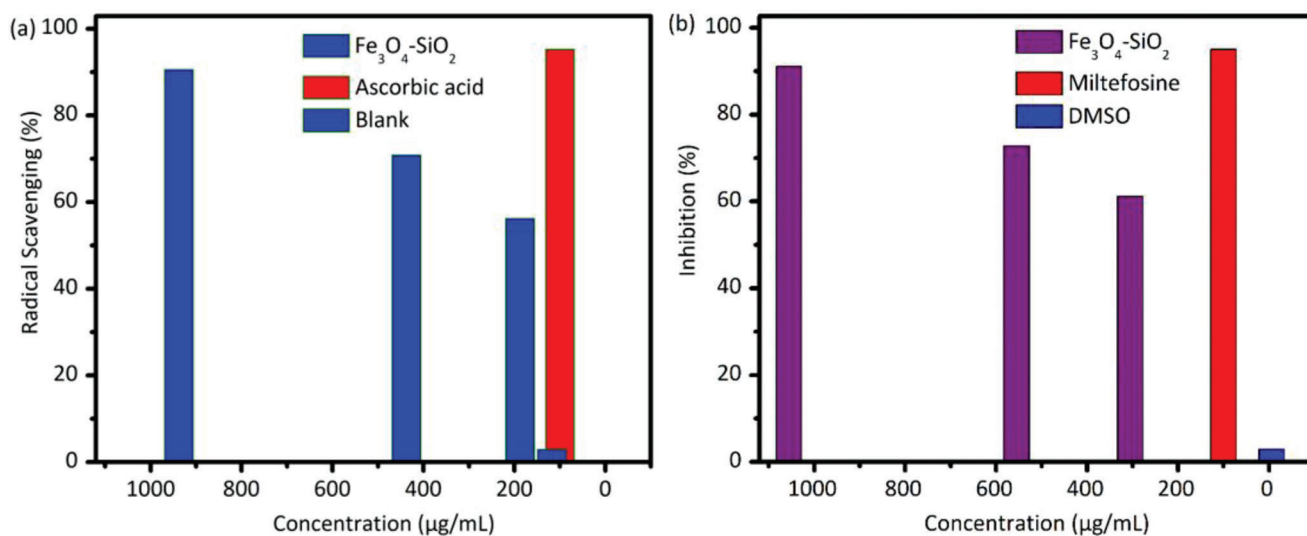


**Figure 13.** a) Antioxidant and b) antileishmanial activity of Fe<sub>3</sub>O<sub>4</sub>-SiO<sub>2</sub> nanocomposite.

**Table 5.** Summary of the antioxidant and antileishmanial activities of  $\text{Fe}_3\text{O}_4\text{-SiO}_2$  nanocomposite.

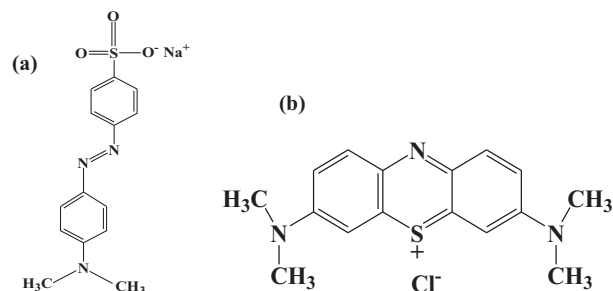
Sample	Antioxidant activity		
	Concentration [ $\mu\text{g mL}^{-1}$ ]	% Activity	$\text{IC}_{50}$ [ $\mu\text{g mL}^{-1}$ ]
Standard (Ascorbic acid)	100	95.27%	$201.10 \pm 0.50$
$\text{Fe}_3\text{O}_4\text{-SiO}_2$	250	56.24%	
-do-	500	78.83%	
-do-	1000	90.55%	
Sample	Antileishmanial activity		
	Concentration [ $\mu\text{g mL}^{-1}$ ]	% Activity	$\text{IC}_{50}$ [ $\mu\text{g mL}^{-1}$ ]
Standard (Miltefosine)	100	95.05%	$157.47 \pm 0.51$
$\text{Fe}_3\text{O}_4\text{-SiO}_2$	250	61.15%	
-do-	500	72.79%	
-do-	1000	91.12%	

in the order of  $1000 > 500 > 250 \mu\text{g mL}^{-1}$ . This clearly demonstrates that the higher the concentrations, the higher will be the antioxidant activity.

Similarly, the antileishmanial activity of the synthesized nanocomposite was also performed, and the results are shown in Table 5 and Figure 13b. In this case, DMSO was used as a negative control and Miltefosine as a reference drug. The previous literature<sup>[41]</sup> indicates that the antileishmanial activity increases with the increase in concentration, that is, at a higher concentration, the antileishmanial activity is greater, and vice versa. Figure 13b reveals that as the concentration of the solution increases, the antileishmanial activity of the nanocomposite enhances. The antileishmanial activity of the nanocomposite at different concentrations is in the order of  $1000 > 500 > 250 \mu\text{g mL}^{-1}$ .

### 3. Conclusion

The  $\text{Fe}_3\text{O}_4\text{-SiO}_2$  nanocomposite was prepared through an easily handed co-precipitation and Stober methods, using ferric chloride hexahydrate ( $\text{FeCl}_3 \cdot 6\text{H}_2\text{O}$ ), ferrous chloride tetrahydrate ( $\text{FeCl}_2 \cdot 4\text{H}_2\text{O}$ ) as  $\text{Fe}_3\text{O}_4$  precursors in 2:1 ratio,  $\text{NH}_3$  solution as a precipitating agent, water as a solvent, and TEOS as  $\text{SiO}_2$  precursor. The ratio of  $\text{Fe}_3\text{O}_4$  to TEOS was 1:5 and a ratio of 1:1:20:6 of  $\text{Fe}_3\text{O}_4$ , TEOS, ethanol, and deionized water was used in the synthesis of the  $\text{Fe}_3\text{O}_4\text{-SiO}_2$  nanocomposite. The structure, morphology, crystallinity, and stability of the nanocomposite have been confirmed by various characterization techniques such as UV, SEM, TEM, FTIR, XRD, and DSC TGA. The direct band-gap energy of the nanocomposite was also calculated as  $E_g = 1.75 \text{ eV}$  which is in close agreement with the already reported works. The nanocomposite was applied as a catalyst for the catalytic and photocatalytic activities of MB and MO dyes in aqueous media. The catalytic/photocatalytic activities of both dyes were also compared using the same nanocomposite  $\text{Fe}_3\text{O}_4\text{-SiO}_2$ . It is confirmed that the  $\text{Fe}_3\text{O}_4\text{-SiO}_2$  composite has best catalytic and photocatalytic activities for MB dye with degradation efficiency of 91% and 93% relative to the MO with 35% and 51%. Besides, MB could be rapidly degraded compared to the MO, as indicated by their  $k$ -values. Moreover, this different behavior of MB and MO toward



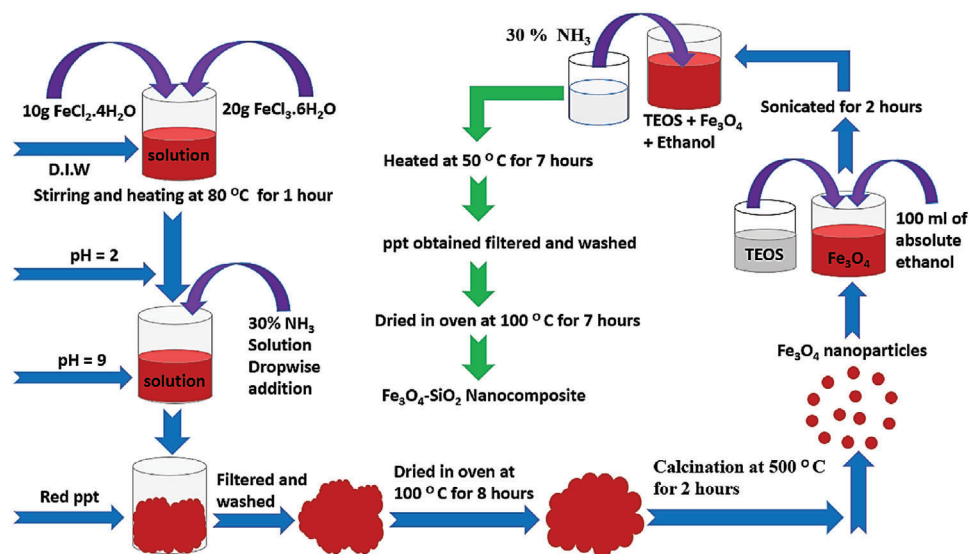
**Scheme 1.** Chemical structures of a) methyl orange (MO) and b) methylene blue (MB).

the same catalyst in their reactivity may be due to their different chemical nature, structures, and interaction with the same nanocomposite. A comparison of the current results and their relation with the previous work suggests that photodegradation of the dyes is greatly affected by various experimental variables such as the nature of the catalyst and pollutant, amount of the catalyst and pollutant, pH, and temperature of the reaction medium, quality of light, and presence of additional precursors in the solution. One of the feasible reasons for the faster degradation of MB in contrast to MO is the involvement of both the holes and hydroxyl radical, whereas, for MO, the formation of holes proved to be the most essential factor. The kinetic study suggests that this removal process follows a pseudo-first-order kinetic. The recycling performance of the composite was tested in the dye removal process for four continuous cycles, and no apparent change is found in the removal efficiency, which reflects the stability of the composite. Moreover, the nanocomposite has shown appreciable antioxidant and antileishmanial activities even at very low concentrations. These activities are further improved by the concentration of the nanocomposite in the solution. Finally, we suggest that this material can be used to remove pollutants and pathogens from wastewater with high efficiency and stability.

### 4. Experimental Section

**Materials:** All chemicals used in the preparation of  $\text{Fe}_3\text{O}_4$ ,  $\text{Fe}_3\text{O}_4\text{-SiO}_2$  materials were of analytical grade. Ferric chloride hexahydrate ( $\text{FeCl}_3 \cdot 6\text{H}_2\text{O}$  Sigma-Aldrich), ferrous chloride tetrahydrate ( $\text{FeCl}_2 \cdot 4\text{H}_2\text{O}$  Sigma-Aldrich), ammonia solution ( $\text{NH}_3$  30% Merck), absolute ethanol ( $\text{C}_2\text{H}_5\text{OH}$ , Sigma-Aldrich) were used. The molecular formulas for MO and MB are  $\text{C}_{14}\text{H}_{14}\text{N}_3\text{NaO}_3\text{S}$  and  $\text{C}_{16}\text{H}_{18}\text{ClN}_3\text{S}$ , respectively, and their chemical structures are shown in **Scheme 1**.

**Synthesis and Characterization of  $\text{Fe}_3\text{O}_4\text{-SiO}_2$  Nanocomposite:** The Stober method was used to fabricate  $\text{Fe}_3\text{O}_4\text{-SiO}_2$ . In a typical experiment, the nanocomposite was prepared in 1:1:20:6 molar ratio, that is, adding 5 g of  $\text{Fe}_3\text{O}_4$ , 5 mL of TEOS, and 30 mL deionized water (DIW) in 100 mL of absolute ethanol. This mixture was well sonicated for about 2 h to obtain a uniform dispersion. Thereafter, 30% of the  $\text{NH}_3$  solution was slowly added under constant stirring and then the solution was heated for 7 h at  $50^\circ\text{C}$  at 600 rpm. The  $\text{Fe}_3\text{O}_4\text{-SiO}_2$  nanocomposite was obtained and filtered using the Whatman No. 1 filter paper. The residue was washed several times with DIW and absolute ethanol and then dried in an oven at  $100^\circ\text{C}$  for 7 h. After this, it was ground into fine powdered with the help of mortar and pestle and stored in a sealed bottle. Some other samples of  $\text{Fe}_3\text{O}_4\text{-SiO}_2$  nanocomposite, using various amounts of  $\text{Fe}_3\text{O}_4$  and TEOS, that is, 1:1, 1:2, 1:3, 1:4, and 1:5 were also obtained. **Scheme 2** shows the pictorial representation of various steps for the synthesis of



**Scheme 2.** Schematic representation for the synthesis of  $\text{Fe}_3\text{O}_4\text{-SiO}_2$  nanocomposite.

$\text{Fe}_3\text{O}_4\text{-SiO}_2$  nanocomposite. The  $\text{Fe}_3\text{O}_4\text{-SiO}_2$  nanocomposites were characterized by UV-vis and FTIR spectrophotometers, SEM, EDX, TEM, XRD, DSC, and TGA for their structure elucidation, morphology, crystallinity, and stability.

**Photocatalytic Degradation:** The final products of  $\text{Fe}_3\text{O}_4\text{-SiO}_2$  nanocomposites were employed in catalysis and photocatalysis toward the degradation/removal of MB and MO dyes from wastewater under UV-light irradiation using a 125 W Hg-vapor lamp as a light source. It was also coated to prevent light dispersion and to concentrate it on the reaction process. Various experiments were brought about by taking the specific amounts of  $\text{Fe}_3\text{O}_4\text{-SiO}_2$  composite (0.1 g) in 100 mL of 20 ppm solution of MB and MO with the constant stirring condition. In a typical experiment, before exposing the dye solution to UV-light irradiation, the equilibrium between adsorbed and desorbed dye molecules on the surface of  $\text{Fe}_3\text{O}_4\text{-SiO}_2$  nanocomposites was confirmed by stirring the mixture in the dark for 1 h. A given amount of dye solution was collected at a regular interval of time and centrifuged at 4000 rpm for 5–10 min. The photocatalytic degradation of the dyes was assessed by measuring their maximum absorbance wavelength using a double beam UV-vis spectrophotometer (Cary 100 Bio); while the percentage degradation of the MB and MO dyes were estimated using Equation (5)

$$\text{Degradation Rate (\%)} = \left( \frac{A_0 - A_t}{A_0} \right) \times 100 \quad (5)$$

where " $A_0$ " and " $A_t$ " are respectively the absorbances of dye solutions, initially and at a certain reaction time  $t$  (min); the absorbance representing the corresponding concentrations of the dye solutions. The removal efficiency was also calculated using Equation (6).

$$\text{Removal efficiency } (Q_t) = \left( \frac{A_0 - A_t}{M} \right) \times V \quad (6)$$

where  $Q_t$  is the removal efficiency ( $\text{mg g}^{-1}$ ),  $V$  (L) is the volume of the mixture,  $M$  (g) is the amount of nanocomposite, while  $A_0$  ( $\text{mg L}^{-1}$ ) and  $A_t$  ( $\text{mg L}^{-1}$ ) are the initial and final concentrations (concentration at time =  $t$ ). The concentrations of solution were traced from the corresponding values of absorbance of the dye solutions using the Beer-Lambert law.

**Antioxidant Activity of  $\text{Fe}_3\text{O}_4\text{-SiO}_2$  Nanocomposite:** For  $\text{Fe}_3\text{O}_4\text{-SiO}_2$  nanocomposite, a previously developed method (1,1-diphenyl-

2-picrylhydrazyl [DPPH] assay) had been used to induce antioxidant activity.<sup>[41]</sup> The  $\text{Fe}_3\text{O}_4\text{-SiO}_2$  nanocomposite with different concentrations (such as 250, 500, and 1000  $\mu\text{g mL}^{-1}$ ) was prepared and ascorbic acid served as a reference point for quality control. About 1 mL of each  $\text{Fe}_3\text{O}_4\text{-SiO}_2$  nanocomposite (250, 500, and 1000  $\mu\text{g mL}^{-1}$ ) was mixed with 1 mL of the DPPH solution (0.12 mM) prepared in methanol and an additional 4 mL methanol was added to it and kept in the dark for 40 min. Afterward, the absorbance of the solution was estimated at a wavelength of 516 nm. Moreover, the IC50 values of the composite were also estimated and compared at different concentrations. The scavenging percentage of DPPH was determined via the Equation (7) given below.

$$\text{Radical Scavenging (\%)} = \frac{1 - A_a - A_b}{A_c} \times 100 \quad (7)$$

Where, " $A_a$ ," " $A_b$ " indicates the absorbance of composite in the presence, as well as the absence of DPPH, and " $A_c$ ," denotes the absorbance of the control solution.

The antileishmanial activity of the synthesized  $\text{Fe}_3\text{O}_4\text{-SiO}_2$  nanocomposite was also carried out via the previously established method in ref. [41]. In this method, the nanocomposite of  $\text{Fe}_3\text{O}_4\text{-SiO}_2$  was subjected to screen its leishmanicidal potential while using 10% Fetal Bovine Serum (FBS), 1% Miltefosine (antibiotic), and 1% Hepes (*N*-hydroxyethylpiperazine-*N'*-ethane sulfonic acid) buffered RPMI-1640 medium for Leishmania tropical promastigotes. Then, using a Neubauer chamber, the enter log phase was started and developed until 5–6 million cells per mL were seen. The nanocomposite was taken in 96-well plates with various concentrations, that is, 1000, 500, and 250  $\mu\text{g mL}^{-1}$ , and was screened in triplicate. A powerful inactivator of leishmania Miltefosine was utilized as a reference drug in this technique, and the composite was solubilized in a 0.5 percent solution of dimethyl sulfoxide (DMSO), which served as a negative control. The plate was seeded with 100  $\mu\text{L}$  of full culture media that included  $10^4$  cells per well which had previously been pre-treated with the screening composite at the required concentrations. The 96-well plate was left incubated at 25 °C for 72 h. Treated promastigotes of the nanocomposite were examined through the tetrazolium-dye (MTT) colorimetric technique. A 100  $\mu\text{L}$  of MTT dye prepared in PBS was added to each well of 96-well plates and was left incubated for 3 h at 37 °C. After the incubation period, 40  $\mu\text{L}$  of DMSO was added to each of the well plates as a stopping solution, and the plate reading was measured at 570 nm with the help of an ELISA Biotek plate reader.



The percentage inhibition of the compounds was estimated via the following Equation (8).

$$\text{Inhibition (\%)} = \frac{\text{Mean OD of sample} - \text{Mean OD of blank}}{\text{Mean OD of positive control} - \text{Mean OD of blank}} \times 100 \quad (8)$$

## Acknowledgements

The authors acknowledge the Faculty of Environment, Science and Economy, University of Exeter, UK, and funding support from Engineering and Physical Sciences Research Council (EPSRC).

After initial online publication, the second affiliation of author A.K. was corrected to the Department of Mathematics and Sciences, Faculty of Humanities and Sciences, Prince Sultan University, on February 27, 2023, due to a previous error.

## Conflict of Interest

The authors declare no conflict of interest.

## Data Availability Statement

The data that support the findings of this study are available from the corresponding author upon reasonable request.

## Keywords

catalysis, Fe<sub>3</sub>O<sub>4</sub>-SiO<sub>2</sub>, photocatalysis, pollutants, wastewater treatments

Received: December 20, 2022

Revised: February 3, 2023

Published online:

- [1] M. Humayun, W. Pi, Y. Yuan, L. Shu, J. Cao, A. Khan, Z. Zheng, Q. Fu, Y. Tian, W. Luo, *J. Colloid Interface Sci.* **2021**, 599, 484.
- [2] M. Humayun, Z. Hu, A. Khan, W. Cheng, Y. Yuan, Z. Zheng, Q. Fu, W. Luo, *J. Hazard. Mater.* **2019**, 364, 635.
- [3] M. Humayun, Y. Qu, F. Raziq, R. Yan, Z. Li, X. Zhang, L. Jing, *Environ. Sci.* **2016**, 50, 13600.
- [4] M. Yaseen, M. Humayun, A. Khan, M. Idrees, N. Shah, S. Bibi, *Molecules* **2022**, 27, 5343.
- [5] M. Humayun, H. Ullah, M. Usman, A. Habibi-Yangjeh, A. A. Tahir, C. Wang, W. Luo, *J. Energy Chem.* **2022**, 66, 314.
- [6] M. Humayun, C. Wang, W. Luo, *Small Methods* **2022**, 6, 2101395.
- [7] M. Humayun, F. Raziq, A. Khan, W. Luo, *Green Chem. Lett. Rev.* **2018**, 11, 86.
- [8] A. P. Kumar, D. Bilehal, T. Desalegn, S. Kumar, F. Ahmed, H. C. A. Murthy, D. Kumar, G. Gupta, D. K. Chellappan, S. K. Singh, K. Dua, Y. -I. Lee, *Adsorpt. Sci. Technol.* **2022**, 2022, 3970287.
- [9] S. Ali, M. Humayun, W. Pi, Y. Yuan, M. Wang, A. Khan, P. Yue, L. Shu, Z. Zheng, Q. Fu, W. Luo, *J. Hazard. Mater.* **2020**, 397, 122708.
- [10] M. Humayun, M. He, W. Feng, C. Jin, Z. Yao, Y. Wang, W. Pi, S. Ali, A. Khan, M. Wang, Z. Zheng, Q. Fu, H. Xia, W. Luo, *Sol. Energy* **2021**, 215, 121.
- [11] F. Liu, F. Niu, N. Peng, Y. Su, Y. Yang, *RSC Adv.* **2015**, 5, 18128.
- [12] A. Kunzmann, B. Andersson, C. Vogt, N. Feliu, F. Ye, S. Gabrielsson, M. S. Toprak, T. Buerki-Thurnherr, S. Laurent, M. Vahter, H. Krug, M. Muhammed, A. Scheynius, B. Fadeel, *Toxicol Appl Pharmacol* **2011**, 253, 81.
- [13] K. KH, *Int. J. Mater. Sci. Appl.* **2014**, 3, 147.
- [14] M. Khan, R. Khattak, A. Khan, Q. Chen, J. Nisar, Z. Iqbal, A. Rashid, A. Kamran, I. Zekker, M. Zahoor, K. Alzahrani, G. Batiha, *Molecules* **2021**, 26, 3440.
- [15] N. L. Olteanu, C. A. Lazăr, A. R. Petcu, A. Meghea, E. A. Rogoza, M. Mihaly, *Arab J Chem* **2016**, 9, 854.
- [16] X. Li, Z. Yang, N. Hu, L. Zhang, Y. Zhang, L. Yin, *Chem* **2016**, 6, 48379.
- [17] N. Bellotti, R. Arrechea, M. Blancoa, P. Vázquez, *Procedia Mater. Sci.* **2015**, 9, 627.
- [18] Q. H. F. Rebelo, C. S. Ferreira, P. L. Santos, J. A. Bonacin, R. R. Passos, L. A. Pocrifka, M. M. S. Paula, *Part. Sci. Technol.* **2019**, 37, 911.
- [19] M. Yaseen, S. Farooq, A. Khan, N. Shah, L. A. Shah, S. Bibi, I. U. Khan, S. Ahmad, *Chem* **2022**, 69, 1637.
- [20] D. H. K. Munasir, N. P. P. Sunaryono, N. Hidayat, A. Taufiq, Z. A. Imam Supardi, *J. Phys. Conf. Ser.* **2018**, 1093, 012015.
- [21] K. K. Jena, H. Mittal, V. S. Wadi, G. K. Mani, S. M. Alhassan, *ACS Appl. Mater. Interfaces* **2019**, 11, 30247.
- [22] M. I. Mobarakeh, A. Saffar-Teluri, S. A. H. Tabrizi, *Res. Chem. Intermed.* **2015**, 41, 6625.
- [23] T. Dippong, O. Cadar, E. A. Levei, I.-G. Deac, G. Borodi, *Ceram. Int.* **2018**, 44, 10478.
- [24] M. González-Hurtado, J. A. Marins, B. G. Soares, J. R. Briones, A. R. Rodríguez, E. Ortiz-Islas, *Rev. Adv. Mater. Sci.* **2018**, 55, 12.
- [25] X. Wang, L. Wang, Q. Su, J. Zheng, *Compos. Sci. Technol.* **2013**, 89, 52.
- [26] M. Sonmez, M. Georgescu, L. Alexandrescu, D. Gurau, A. Fica, D. Fica, E. Andronescu, *Curr. Pharm. Des.* **2015**, 21, 5324.
- [27] W. Wu, Q. He, C. Jiang, *Nanoscale Res. Lett.* **2008**, 3, 397.
- [28] C. Hui, C. Shen, J. Tian, L. Bao, H. Ding, C. Li, Y. Tian, X. Shi, H.-J. Gao, *Nanoscale* **2011**, 3, 701.
- [29] T. Etemadina, A. Allahrasani, B. Barikbin, *Polym. Bull.* **2019**, 76, 6089.
- [30] C. Fu, X. Liu, Y. Wang, L. Li, Z. Zhang, *RSC Adv.* **2019**, 9, 20256.
- [31] R. Wo, Q.-L. Li, C. Zhu, Y. Zhang, G.-f. Qiao, K.-y. Lei, P. Du, W. Jiang, *J. Chem. Eng. Data* **2019**, 64, 2455.
- [32] M. A. Ebrahimzadeh, S. Mortazavi-Derazkola, M. A. Zazouli, *J. Mater. Sci.: Mater. Electron.* **2019**, 30, 10994.
- [33] M. Khoshnam, H. Salimijazi, *Surf. Interfaces* **2021**, 26, 101322.
- [34] M.-P. Mazhari, M. Hamadianian, *J. Electron. Mater.* **2018**, 47, 7484.
- [35] A. Nikmah, A. Taufiq, A. Hidayat, *IOP Conf. Ser.: Earth Environ. Sci.* **2019**, 276, 012046.
- [36] G. Purwandono, I. s Fatimah, I. Sahroni, P. W. Citradewi, A. Kamari, S. Sagadevan, W.-C. Oh, R.-A. n Doong, *Green Process. Synth.* **2022**, 11, 345.
- [37] X. Lv, W. Huang, X. Ding, J. He, Q. Huang, J. Tan, H. Cheng, J. Feng, L. Li, *J. Rare Earths* **2020**, 38, 1288.
- [38] S. Narzary, K. Alamelu, V. Raja, B. M. Jaffar Ali, *J. Environ. Chem. Eng.* **2020**, 8, 104373.
- [39] M. Makeswari, P. Saraswathi, *SN Appl. Sci.* **2020**, 2, 336.
- [40] L. V. Trandaflović, D. J. Jovanović, X. Zhang, S. Ptašniška, M. D. Dramićanin, *Appl. Catal. B* **2017**, 203, 740.
- [41] M. Yaseen, S. Farooq, A. Khan, N. Shah, L. A. Shah, S. Bibi, I. U. Khan, S. Ahmad, *J. Chin. Chem. Soc.* **2022**, 69, 1637.
- [42] D. Rehana, D. Mahendiran, R. S. Kumar, A. K. Rahiman, *Biomed. Pharmacother.* **2017**, 89, 1067.